PCCP



PAPER



Cite this: Phys. Chem. Chem. Phys., 2017, 19, 29549

and HNO revealed by ab initio quantum chemical investigations†

Hidden complexities in the reaction of H_2O_2

Daniel Beckett, D Marc Edelmann, Jonathan D. Raff D and Krishnan Raghavachari*

Nitroxyl (HNO) and hydrogen peroxide have both been implicated in a variety of reactions relevant to environmental and physiological processes and may contribute to a unique, unexplored, pathway for the production of nitrous acid (HONO) in soil. To investigate the potential for this reaction, we report an in-depth investigation of the reaction pathway of H₂O₂ and HNO forming HONO and water. We find the breaking of the peroxide bond and a coupled proton transfer in the first step leads to hydrogen nitryl (HNO₂) and an endogenous water, with an extrapolated NEVPT2 (multireference perturbation theory) barrier of 29.3 kcal mol⁻¹. The first transition state is shown to possess diradical character linking the far peroxide oxygen to the bridging, reacting, peroxide oxygen. The energy of this first step, when calculated using hybrid density functional theory, is shown to depend heavily on the amount of Hartree-Fock exchange in the functional, with higher amounts leading to a higher barrier and more diradical character. Additionally, high amounts of spin contamination cause CCSD(T) to significantly overestimate the TS1 barrier with a value of $36.2 \text{ kcal mol}^{-1}$ when using the stable UHF wavefunction as the reference wavefunction. However, when using the restricted Hartree-Fock reference wavefunction, the TS1 CCSD(T) energy is lowered to yield a barrier of 31.2 kcal mol⁻¹, in much better agreement with the NEVPT2 result. The second step in the reaction is the isomerization of HNO2 to trans-HONO through a Grotthuss-like mechanism accepting a proton from and donating a proton to the endogenous water. This new mechanism for the isomerization of HNO2 is shown to have an NEVPT2 barrier of 23.3 kcal mol⁻¹, much lower than previous unimolecular estimates not including an explicit water. Finally, inclusion of an additional explicit water is shown to lower the HNO2 isomerization barrier even further.

Received 29th August 2017, Accepted 16th October 2017

DOI: 10.1039/c7cp05883g

rsc.li/pccp

1. Introduction

Nitroxyl (HNO) is postulated to be a key intermediate in numerous reaction pathways involving the oxidation of nitrogen during combustion, 1,2 atmospheric chemistry, microbial nitrification,⁴ pollution control,^{5,6} and physiological processes.⁷ Recently, there is interest in the potentially large contribution of soil microbial nitrification processes as a source of reactive oxides of nitrogen such as NO_x ($NO_x = NO + NO_2$)⁸⁻¹⁰ and nitrous acid $(HONO)^{11-13}$ to the atmosphere, which may account for $\sim 15\%$ of global emissions of NO_x and play a key role in tropospheric ozone and aerosol formation.¹⁴ Formation of NO_x and HONO in soil is a byproduct of microbial nitrification in which the enzyme ammonia monooxygenase (AMO) converts ammonia to hydroxylamine and

Department of Chemistry, Indiana University, Bloomington, Indiana, 47405, USA. E-mail: kraghava@indiana.edu

hydroxylamine oxidoreductase (HAO) converts hydroxylamine to nitrite, 15 in a process involving the HNO intermediate. 10

Pollution control technology aimed at eliminating ammonia from agricultural waste and runoff or removing NOx from combustion exhaust are other areas where HNO chemistry plays a role. For example, the reaction of ammonia with O2 on certain catalysts [i.e., selective catalytic oxidation (SCO)] is thought to yield an HNO intermediate.⁶ Advanced oxidation processes utilizing photoactive catalysts, H2O2 photolysis, ozone treatment, and electrolysis have been applied to removal of N-waste from aquatic systems. 16 Applicable to these systems, Chen et al. have proposed HNO as an intermediate in the oxidation of hydroxylamine and its derivatives by H₂O₂. ¹⁷ In these processes, reactions between HNO and reactive oxygen species can potentially lead to oxidized byproducts such as NO_x and N2O, the latter of which is a potent greenhouse gas and ozone depleting substance in the stratosphere. 18

Nitroxyl also plays an important role in biochemistry. 19 Although there is an ongoing debate on whether nitroxyl is produced endogenously, free HNO has been proposed as a

[†] Electronic supplementary information (ESI) available. See DOI: 10.1039/ c7cp05883g

precursor to NO during certain enzymatic processes.^{20,21} In medicine, there has been a great deal of research within the past decade into nitroxyl's unique ability to prevent heart attacks through lowering cardiac preload and diastolic pressure without increasing arterial resistance.^{21,22} Additionally, early application of nitroxyl has been shown to prevent oxidative damage to cells during ischemia reperfusion injury, *i.e.* before deoxygenated cells are reoxygenated.²³ However, application of nitroxyl during the process of reoxygenation increases the degree of damage, potentially through reaction with reactive oxygen species, such as hydrogen peroxide, which are formed during the process.^{24,25}

Although HNO plays a recognized role in environmental and biochemical processes, little is known about its chemistry. This is primarily due to the challenges in studying this reactive molecule experimentally. In higher concentrations, the fate of HNO is to dimerize and subsequently decompose to N₂O.²⁶ Relative to the dimerization pathway, oxidation of HNO by O₂ under physiological conditions is slow.²⁷ However, metabolic processes are active in converting O2 to reactive oxygen intermediates such as H₂O₂, which may be more reactive toward HNO than O2. Hydrogen peroxide is also produced through oxidative stress and is involved in a number of signaling processes in the body.²⁸ Moreover, H₂O₂ is also an important oxidant used in advanced oxidation treatments of N-containing waste. Presently, it is unknown whether HNO can react with H2O2 and, if it does, whether it can be a source of NO_x or HONO to environmental or physiological

The goal of this work is to determine the lowest energy reaction pathway of nitroxyl and hydrogen peroxide. Though the chosen system is relatively small and seemingly free of complex nonlocal interactions, investigation with electronic structure theory leads to several novel findings. We find the first transition state to be an open shell singlet diradical, requiring a more nuanced approach than simple density functional theory. In particular, different hybrid density functionals yield a wide range of barriers for the first transition state, depending entirely on the amount of Hartree-Fock exchange included in the chosen functional. The amount of Hartree-Fock exchange increases the diradical character of the transition state, an effect local density functional theory fails to reproduce. Additionally, we show that even the correlated CCSD(T) and BD(T) methods mistreat this transition state when using the stable UHF wavefunction as a reference and that the RHF wavefunction must be used to obtain reliable results. We have also demonstrated that the water molecule released from the first step substantially lowers the barrier for the subsequent rearrangement step, yielding a barrier much lower than those reported in previous studies of the rearrangement in an unsolvated environment.

In the following section we describe the Computational methods and theory used in the paper. Results and discussion is divided into three parts: determination of a B3LYP singlet reaction pathway, investigation of the pathway with a variety of functionals and elucidation of the effect of exact exchange in

the initial barrier of the reaction, and finally an NEVPT2//CASSCF investigation of the obtained barriers.

2. Computational methods and theory

The Gaussian 09 program suite²⁹ has been used for all calculations in this work except for the CASSCF and NEVPT2 calculations, which were performed using ORCA.³⁰ All reported structures were optimized on the singlet surface using the B3LYP³¹⁻³³ density functional with the aug-cc-pVQZ basis set.34 Unrestricted wavefunctions are obtained in all cases where the closed shell solutions possess an instability, specifically in the case of TS1 and the reactant complex. Vibrational analysis was carried out at the B3LYP/aug-cc-pVOZ level to confirm the nature of the minima and to obtain zero-point corrected energies and Gibbs free energies. All transition states were linked to the corresponding products and reactants using intrinsic reaction coordinate (IRC)³⁵⁻³⁷ analysis at the B3LYP/ aug-cc-pVTZ level of theory. The ends of IRC calculations were then optimized with tight convergence criteria to obtain the corresponding intermediate local minima, referred to as Int#. For TS1, the barrier is calculated with respect to the reactant complex to provide a more comprehensive picture of the energy required to initiate this reaction. The other barriers were calculated with respect to the appropriate reaction intermediates as seen in Fig. 1 of the Results and discussion. To explore the possibility of transition states being stabilized by solvation effects, all structures were further optimized, and frequencies obtained, at the B3LYP/aug-cc-pVQZ level of theory using the CPCM implicit solvent model with water as the solvent molecule and a corresponding dielectric constant of 78.36. 38,39

To analyze the functional-dependence of the reported barriers, all structures were additionally optimized with unrestricted versions of Zhao and Truhlar's M06-2X hybrid functional, 40 Adamo and Barone's PBE0 hybrid functional, 41 the dispersion-corrected B3LYP-D3BJ (using Grimme et al.'s D3 correction42 and Becke-Johnson damping⁴³), the long-range corrected CAM-B3LYP⁴⁴ as well as the associated CAM-B3LYP-D3BJ, and ωB97X-D. 45 The B3LYP/aug-ccpVQZ geometries were used for single point CCSD(T), 46,47 BD(T), 48 CASSCF, and N-Electron Valence Perturbation Theory (NEVPT2)⁴⁹ calculations. CASSCF and NEVPT2 calculations were performed using version 4.0.0.2 of the ORCA computational chemistry program.³⁰ CASSCF calculations were performed with the cc-pVDZ basis set and the optimized wavefunctions were used as reference states for NEVPT2/aug-cc-pVDZ calculations to account for dynamic correlation. For all NEVPT2 calculations, the fully internally contracted (FIC-NEVPT2) algorithm was used. 50 Choosing a proper active space is the most crucial step when setting up any CASSCF calculation and we followed the general guidelines popularized by Veryazov, Malmqvist, and Roos for treating nitrogen-containing systems by including all heavy atom 2p orbitals and all hydrogen 1s orbitals.⁵¹ Thus, the chosen active space was 18 electrons distributed across 15 orbitals (18,15).

Though the studied system is relatively small, the active space is quite large and the direct NEVPT2 calculations were

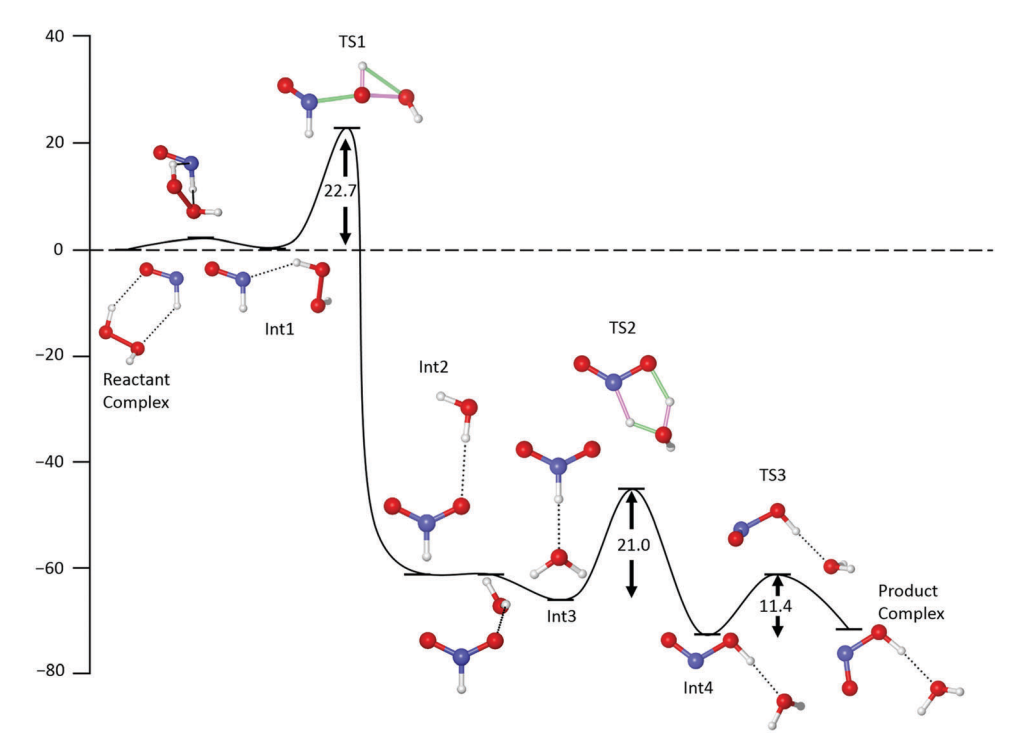


Fig. 1 B3LYP/aug-cc-pVQZ reaction diagram with zero-point corrected energies. Green lines depict forming bonds, magenta lines depict breaking bonds. Energies in kcal mol⁻¹ relative to ground state energy of the reactant complex. Geometries provided in the ESI.†

carried out with the aug-cc-pVDZ basis. To include the larger basis set effects on NEVPT2, we employ an extrapolation procedure by adding the difference between the CCSD(T)/aug-cc-pVTZ barriers and barriers calculated with CCSD(T)/aug-cc-pVDZ, as shown in eqn (1). We consider the NEVPT2 results to be the most accurate reference values to calibrate the performance of other methods in this study. The ESI† contains the aug-cc-pVDZ results for the relevant levels of theory as well as the $\Delta_{\text{aug-cc-pVTZ}}^{\text{aug-cc-pVTZ}}$ for both CCSD(T) and BD(T) using an RHF reference wavefunction, for reasons described in the Results and discussion section.

$$\begin{split} E_{\text{extrapolated}}^{\text{NEVPT2}} &= E_{\text{aug-cc-pVDZ}}^{\text{NEVPT2}} + \left(E_{\text{aug-cc-pVTZ}}^{\text{CCSD(T)}} - E_{\text{aug-cc-pVDZ}}^{\text{CCSD(T)}}\right) \\ &= E_{\text{aug-cc-pVDZ}}^{\text{NEVPT2}} + \varDelta_{\text{aug-cc-pVDZ}}^{\text{aug-cc-pVDZ}} \end{split} \tag{1}$$

Due to large differences in barrier height across the examined levels of theory, the transition state labeled TS1 was subject to additional analysis. First, the barrier for the transition state was calculated with the considered density functionals using the Yamaguchi spin projection procedure for diradicals, outlined in eqn (2) and (3). 52,53 Here, the spin-projected energy, $^{1}E_{(SP)}$, is obtained by adding the energy of the singlet-triplet gap to the unrestricted singlet energy, ${}^{1}E_{\text{(USCF)}}$, scaled by an approximate spin contamination fraction, f_{SC} , derived from the singlet and triplet $\langle S^2 \rangle$ values.

$${}^{1}E_{\text{(SP)}} = {}^{1}E_{\text{(USCF)}} + f_{\text{SC}}[{}^{1}E_{\text{(USCF)}} - {}^{3}E_{\text{(USCF)}}]$$
 (2)

$$f_{\rm SC} \approx \frac{{}^{1}\langle S^{2}\rangle}{{}^{3}\langle S^{2}\rangle - {}^{1}\langle S^{2}\rangle}$$
 (3)

Lastly, the percentage of exact Hartree-Fock exchange is implicated in the differing TS1 barriers across the multiple

hybrid density functionals. To elucidate the effect of exact exchange, parameter a in eqn (4) was varied from its typical value of 0.20 to produce modified versions of the B3LYP functional with different amounts of Hartree-Fock exchange, $E_{\rm x}^{\rm HF}$. The other two parameters, b and c, were left at the B3LYP values of 0.72 and 0.81. The modified functionals are referred to as B3LYP[X] where "X" represents the percentage of exact Hartree-Fock exchange. Optimizations were performed with the percent of exact exchange varying from 0 to 40% for TS1 and the associated reactant complex. This same procedure was employed recently in a study of the oxyl character of Mn^V=O and herein we present an application of this technique to a nonmetallic system.54

$$E_{\rm B3LYP} = (1-a)E_{\rm x}^{\rm LDA} + aE_{\rm x}^{\rm HF} + b\Delta E_{\rm x}^{\rm B} + (1-c)E_{\rm c}^{\rm LDA} + cE_{\rm c}^{\rm LYP} \tag{4}$$

Results and discussion

3.1. B3LYP reaction pathway

Fig. 1 presents the full reaction pathway calculated on the singlet surface using B3LYP/aug-cc-pVQZ and zero-point corrected energies. All geometries presented in Fig. 1 can be found in the ESI.† The first reactant complex represents the most favorable interaction between the two reactants, with the hydrogen peroxide donating one hydrogen bond to the nitroxyl oxygen and accepting a hydrogen bond from the opposite oxygen. The intermediate species, Int1, features the hydrogen peroxide donating one hydrogen bond to the nitroxyl nitrogen and is only 0.15 kcal mol⁻¹ higher in energy than the reactant

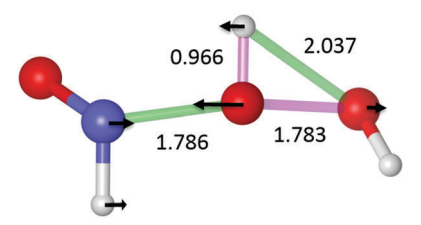


Fig. 2 UB3LYP/aug-cc-pVQZ geometry of TS1 with relevant bond distances reported in Ångströms. Arrows represent relative displacement vectors of the imaginary frequency. Green bonds are forming; magenta bonds are breaking.

complex. The slight reorganization from the reactant complex to Int1 reflects the rearrangement required to prepare the reactants for the chemical reaction to follow. This rearrangement to Int1 is shown in Fig. 1 as the first unlabeled transition state and has a barrier of 2.1 kcal mol⁻¹. The low energy of this transition state is an effect of the shift in the hydrogen bond acceptor on nitroxyl from oxygen to the less favored nitrogen. Due to the low energy of this first transition state, it is not discussed further in this paper and focus is aimed at transition states with more appreciable barriers.

The UB3LYP/aug-cc-pVQZ geometry of the first substantial transition state can be seen in Fig. 2. This is the only transition state with appreciable open shell character and must be treated with an unrestricted wavefunction at the B3LYP level of theory. The normal mode of the imaginary frequency of TS1 features a much longer displacement vector on the central oxygen, leading to a bond with the nitroxyl nitrogen. The peroxide bond is subsequently broken and the hydrogen belonging to the central oxygen is deposited onto the opposite peroxide oxygen to form a water molecule. At the UB3LYP/aug-cc-pVQZ level of theory, the zero-point corrected energy of this transition state is 22.7 kcal mol⁻¹, potentially accessible in the solution phase at 300 K. The product end of the TS1 IRC optimizes to Int2, which features a hydrogen bond donated by the water molecule to an oxygen of the newly formed hydrogen nitryl (HNO₂). Int2 subsequently rearranges to the more stable (by 4.6 kcal mol⁻¹) Int3 by allowing a water oxygen to accept a hydrogen bond from the more weakly bound hydrogen of HNO₂. The rearrangement from Int2 to Int3 is shown in Fig. 1 by the second unlabeled transition state and has a negligible barrier of only 0.13 kcal mol⁻¹. The low barrier of the transition state linking Int2 to Int3 is a result of a migration of the formed water out of the plane of HNO2, allowing the subsequent switch from hydrogen bond donor to hydrogen bond acceptor. As with the first unlabeled transition state, the transition state linking Int2 to Int3 is not discussed further in the text due to its inconsequential barrier.

Fig. 3 presents three possible candidates for the second labeled transition state, each representing the isomerization of $\rm HNO_2$ to trans-HONO. The barrier for this isomerization has been calculated multiple times in the past but never, to our knowledge, in the presence of an explicit water molecule, thus corresponding most closely to TS2-intra as depicted in Fig. 3C. The zero-point corrected reaction energy of TS2-intra can be

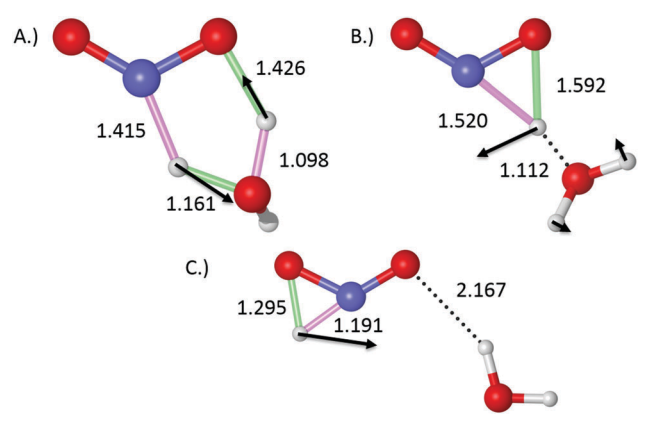


Fig. 3 B3LYP/aug-cc-pVQZ geometries of the three TS2 possibilities. (A) The lowest energy structure, TS2-grott, (B) the second lowest energy, TS2-inter, (C) the highest energy rearrangement, TS2-intra. Arrows represent relative displacement vectors of the imaginary frequency. Relevant bond distances reported in Ångströms. Green bonds are forming; magenta bonds are breaking.

seen in Table 1 to be 52.4 kcal mol⁻¹ and corresponds to the unimolecular shift of the hydrogen atom from the nitrogen to the oxygen of hydrogen nitryl. Since water does not play an active role in assisting the hydrogen shift, we can compare the TS2-intra barrier to previous results *in vacuo*. Our barrier sits too high when compared with the earliest calculated value of 40.9 kcal mol⁻¹ with MRD-CI,⁵⁵ though the more recent barriers for this rearrangement have been reported at 50.7 kcal mol⁻¹ with CCSD(T)/6-311++G(3df,2p).⁵⁷ Recent theoretical exploration of the reaction of nitroxyl and the hydroperoxyl radical (HO₂) reports the isomerization in the presence of a hydroxyl radical to be 47.2 kcal mol⁻¹ at the CBS-Q3 level of theory, sitting within these values.⁵⁸

Compared to all values for the intramolecular arrangement, however, the two transition states directly involving the endogenous water are much lower in energy. TS2-inter, shown in Fig. 3B, features the oxygen of the water acting as a proton shuttle carrying the HNO₂ hydrogen to the *trans*-HONO position with a zero-point corrected energy of 38.3 kcal mol⁻¹. This barrier, while lower than previously reported values, is still quite high. The third form of TS2, shown in Fig. 1 and 3A, is listed as TS2-grott due to its resemblance to the Grotthuss mechanism observed in networks of water molecules. Here, the water

Table 1 B3LYP barriers with and without implicit solvation^a

	B3LYP	CPCM
TS1	22.7	21.3
TS2-grott	21.0	19.7
TS2-inter	38.3	24.9
TS2-inta	52.4	53.9
TS3	11.4	11.5

^a Zero-point corrected energies in kcal mol⁻¹ relative to associated complexes, as illustrated in Fig. 1. Optimizations and frequencies performed at the B3LYP/aug-cc-pVQZ level of theory with and without CPCM solvation as described in Computational methods.

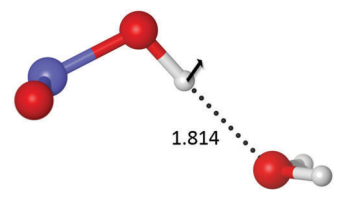


Fig. 4 B3LYP/aug-cc-pVQZ geometry of TS3 with relevant bond distances reported in Ångströms. Arrows represent relative displacement vectors of the imaginary frequency.

molecule receives the HNO₂ proton and subsequently deposits one of its protons onto the oxygen in the *trans*-HONO position. The B3LYP/aug-cc-pVQZ zero-point corrected energy for this transition state was found to be 21.0 kcal mol⁻¹, 18.9 kcal mol⁻¹ lower than the lowest predicted value for the intramolecular rearrangement. Our results suggest the Grotthuss mechanism of TS2-grott is likely the favored mechanism of isomerization of HNO₂ to trans-HONO when water is present as a solvent, not just when water is formed endogenously as it is here.

The final transition state, TS3 as shown in Fig. 4, represents the rotation of the HONO hydrogen to the cis-HONO position. Our value of 11.4 kcal mol⁻¹ for this transition state matches well with the previous value of 9.9 kcal mol⁻¹ reported at the CBS-QB3 level of theory both with⁵⁸ and without a hydroxyl radical.⁵⁹ It should be noted here, the *cis*-HONO conformer is 1.0 kcal mol⁻¹ higher in energy than the *trans* conformer at the reported level of theory and this step is included for the sake of completeness in exploring the reaction pathway. Again, the 1.0 kcal mol⁻¹ stability of the *trans* conformer over the *cis* conformer agrees well with previous results of 0.43 kcal mol⁻¹ with a hydroxyl radical present⁵⁸ and 0.35 kcal mol⁻¹ without.⁵⁹

To complete the unrestricted B3LYP/aug-cc-pVQZ analysis of the full pathway, Table 1 presents the barriers of each labeled transition state optimized with and without CPCM implicit solvation. Due to its presence in environmental and engineered systems, as well as the effect of an explicit water molecule on TS2, water was chosen as the solvent for this step. The TS1 and TS2-grott barriers are lowered by 1.4 and 1.3 kcal mol⁻¹, respectively, when implicit solvent is included. On the other hand, the TS2-intra and TS3 barriers are increased by 1.5 and 0.1 kcal mol⁻¹ respectively. The only change larger than 2 kcal mol⁻¹ occurs in TS2-inter, where implicit solvent lowers the normally inaccessible barrier of 38.3 kcal mol⁻¹ to 24.9 kcal mol⁻¹. While the decrease in the TS2-inter barrier is significant, the resulting barrier is still 5.2 kcal mol⁻¹ higher than TS2-grott. Thus, implicit solvent has a negligible effect on four of the five studied transition states and does not change the ordering of the potential TS2 mechanisms.

At this point it is prudent to examine the effects an additional explicit water may have on the presented transition states, given the amount by which an endogenous water lowers the barrier of TS2. The only clear-cut case where an additional water may lower the barrier is in the proton transfer mechanism of TS2, extending the Grotthuss mechanism to include two waters. In all other transition states presented here, the

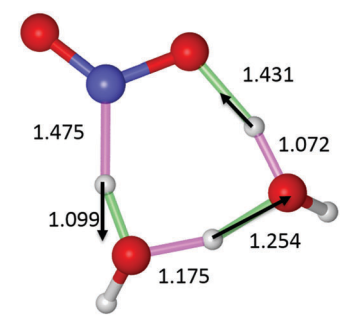


Fig. 5 B3LYP/aug-cc-pVQZ geometry of TS2-grott with an additional explicit water (TS2-grott2x) with relevant bond distances reported in Ångströms. Arrows represent relative displacement vectors of the imaginary frequency.

inclusion of an explicit water is unlikely to significantly alter the mechanism or lower the energy enough to overcome the translational entropy penalty of bringing in an additional water. Fig. 5 presents the transition state resulting from the inclusion of an additional explicit water in TS2-grott, which we will refer to as TS2-grott2x. In TS2-grott2x, the proton transfer is extended such that the abstracting water deposits one of its original protons onto the additional water which in turn transfers one of its protons to form trans-HONO. Table 2 shows the zero-point corrected energy, enthalpy, and Gibbs free energy barriers of TS2-grott and TS2-grott2x in implicit solvent at the B3LYP/aug-cc-pVQZ level of theory. The TS2-grott2x barrier is calculated by subtracting the energy of Int3 and an isolated water molecule from the TS2-grott2x energy. This procedure should accurately reflect the entropy penalty of bringing in an additional water and, as can be seen in Table 2, there is a 13.5 kcal mol⁻¹ increase in the barrier when going from enthalpy to Gibbs free energy. Nevertheless, the Gibbs free energy barrier of TS2-grott2x is only 15.5 kcal mol⁻¹, 6.1 kcal mol⁻¹ lower than TS2-grott. This indicates the two water molecule mechanism in illustrated in Fig. 5 is likely to be a more realistic mechanism of the isomerization of HNO2 to HONO in an aqueous environment. Given the high importance of Gibbs free energy in TS2grott2x and the small difference in barriers of all the other TS2 mechanisms in the treatments to follow, we do not report results of TS2-grott2x at the higher levels of theory explored in this paper, the majority of which only report the electronic energy.

Table 2 TS2-grott B3LYP barriers with explicit water^a

	TS2-grott	TS2-grott2x
ΔE	19.7	4.23
ΔH	18.5	2.00
ΔG	21.6	15.5

^a Zero-point corrected energies, enthalpies, and Gibbs free energies in kcal mol⁻¹ relative to associated complex, as illustrated in Fig. 1. Optimizations and frequencies performed at the B3LYP/aug-cc-pVQZ level of theory with CPCM solvation as described in Computational

Table 3 DFT zero-point corrected barriers^a

	B3LYP	D3BJ	CAM	CAMD3BJ	M062X	PBE0	ωB97XD
TS1	22.7	22.7	28.5	28.6	37.6	25.0	31.0
TS2-grott	21.0	20.2	19.9	19.7	18.9	19.0	21.8
TS2-inter	38.3	37.8	37.5	37.3	36.2	37.6	38.9
TS2-intra	52.4	52.5	53.3	53.4	52.8	52.8	53.4
TS3	11.4	11.3	11.3	11.3	10.4	11.9	11.6

 $[^]a$ Energies in kcal mol^{-1} relative to associated complexes, as illustrated in Fig. 1. Optimizations and frequencies performed at the DFT/aug-cc-pVQZ level of theory.

3.2. TS1, DFT, and the effect of exact exchange

Table 3 presents the zero-point corrected barriers for each transition state in the previous section for the considered density functionals at the DFT/aug-cc-pVQZ level of theory. The most glaring feature of Table 3 is the wide variation in the barrier of the first transition state, TS1. The TS1 barrier varies from 22.7 kcal mol⁻¹ with B3LYP to as high as 37.6 kcal mol⁻¹ with M06-2X, a spread of 14.9 kcal mol⁻¹. Interestingly, there is almost no difference in the barrier of TS1 when including D3BJ dispersion corrections for both B3LYP and CAM-B3LYP. This implies dispersion interactions do not play a significant role in TS1 or the reactant complex and the spread in barrier values across functionals must be arising from some other property.

Aside from TS1, there is very little variation across the other transition state barriers reported in Table 3. Of the remaining transition states, TS2-grott varies the most with a difference of 2.9 kcal mol⁻¹ between M06-2X and ωB97X-D, followed closely by TS2-inter with a spread of 2.7 kcal mol⁻¹. TS2-intra and TS3 do not directly involve the water molecule as in the other TS2 mechanisms and vary by only 1.0 and 1.5 kcal mol⁻¹, respectively. Table 4 reports the Gibbs free energy barriers, at 300 K, for the transition states and the same trends persist. The TS1 barrier increases over the 0 K values by up to 1.2 kcal mol⁻¹, while the relatively constrained TS2-grott and TS2-inter barriers increase by up to 3.0 and 2.2 kcal mol⁻¹, respectively. TS2-intra, which only has one hydrogen bond contact with the endogenous water and is more entropically favored than the other two TS2 mechanisms, actually decreases in activation energy from the 0 K values by up to 1.1 kcal mol^{-1} .

Next, we seek to identify a single component across all density functionals that is responsible for the large variability in the barrier height for TS1 *versus* the other transition states.

Table 4 DFT Gibbs free energy barriers^a

	B3LYP	D3BJ	CAM	CAMD3BJ	M062X	PBE0	ωB97XD
TS1	23.7	23.6	29.3	29.4	38.4	26.0	31.9
TS2-grot	t 23.8	23.2	22.9	22.7	20.7	21.8	24.8
TS2-inte	r 40.3	39.9	39.7	39.5	37.3	39.6	41.1
TS2-intra	a 51.6	52.1	53.2	53.4	51.7	52.1	52.8
TS3	11.7	11.5	11.6	11.5	10.0	12.2	11.7

 $[^]a$ Energies in kcal mol^{-1} relative to associated complexes, as illustrated in Fig. 1. Optimizations and frequencies performed at the DFT/aug-cc-pVQZ level of theory. Gibbs free energies at 300 K.

Table 5 DFT and UHF singlet $\langle S^2 \rangle$ values^a

	B3LYP	рзвј	CAM	CAMD3BJ	M062X	PBE0	ωB97XD	UHF
Reactants	0.14	0.15	0.15	0.15	0.00	0.24	0.00	0.41
TS1	0.53	0.53	0.68	0.68	0.63	0.56	0.63	1.23

^a DFT optimizations performed at the UDFT/aug-cc-pVQZ level of theory. UHF value at aug-cc-pVTZ basis, on the UB3LYP/aug-cc-pVQZ geometries, to correspond with its use in the post-Hartree–Fock methods.

A key point to note in this context is that TS1 is the only transition state in this study with open shell singlet character; the others are closed shell singlets. This means the effect of different functionals on the spin contamination of the open shell species could be a factor in the observed variance. Table 5 reports the $\langle S^2 \rangle$ values of TS1 and the reactant complex across the analyzed functionals on the singlet surface. Table 5 also includes the UHF/aug-cc-pVTZ spin contamination at the UB3LYP/aug-cc-pVQZ geometry, to correspond with the reference wavefunction employed in the post-Hartree-Fock calculations reported later on. Surprisingly, the reactant complex varies more across the individual functionals than TS1, though (aside from the UHF value) the spin contamination is relatively small. The TS1 spin contamination varies by only 0.15 across the different density functionals, but the spin contamination is high enough to demand some sort of treatment. As expected, the UHF spin contamination values are almost twice the highest DFT values for both the reactant complex and TS1, which will prove to be an interesting complication when considering post-Hartree-Fock methods.

Table 6 contains the Mulliken spin densities in TS1, with hydrogens summed into the heavy atoms. Here, the oxygens are numbered from left to right as they appear in Fig. 2. Given this, we observe a modest amount of positive spin density on the nitrogen, nitroxyl oxygen (O1), and the bridging peroxide oxygen (O2), and the corresponding sum of negative spin density on the far peroxide oxygen (O3). The large amount of negative spin density on oxygen 3 implies diradical character and some antiferromagnetic coupling with the bridging oxygen and nitrogen. The positive spin density on the two nitroxyl heavy atoms is linked to the negative spin density of oxygen 3 through the bridging atom to yield, while not a "pure" diradical, certainly a high amount of diradical character that must be considered.

To determine if the various functionals are treating this diradical character in a similar manner, we report the Yamaguchi

Table 6 Mulliken spin densities of TS1^a

Atom	B3LYP	D3BJ	CAM	CAMD3BJ	M062X	PBE0	ωB97XD
N	0.17	0.17	0.14	0.14	0.22	0.15	0.15
O1	0.22	0.22	0.23	0.23	0.19	0.23	0.22
O2	0.13	0.13	0.23	0.23	0.13	0.15	0.19
O3	-0.52	-0.52	-0.60	-0.60	-0.56	-0.53	0.57

^a DFT optimization performed at the UDFT/aug-cc-pVQZ level of theory. Oxygens labeled from left to right in Fig. 2. O1 corresponds to the nitroxyl oxygen, O2 to the peroxide oxygen closest to the nitrogen, O3 to the peroxide oxygen furthest away from the nitrogen. Hydrogens summed into heavy atoms.

Table 7 Yamaguchi spin-projected barriers of TS1^a

	B3LYP	D3BJ	CAM	CAMD3BJ	M062X	PBE0	ωB97XD
TS1	20.5	20.6	26.1	26.0	34.6	23.2	27.6

^a Energies in kcal mol⁻¹ relative to the reactant complex, as illustrated in Fig. 1. Optimizations and frequencies performed at the UDFT/aug-ccpVQZ level of theory. Spin projection performed as specified in eqn (2) and (3) of the Methods section.

spin-projected TS1 barriers in Table 7. Each barrier was obtained by performing a single point calculation on the triplet surface and following eqn (2) and (3) as presented in the Computational methods section for both the reactant complex and TS1. The Yamaguchi procedure lowers the barrier of TS1 by as much as 3.0 kcal mol⁻¹ (in the M06-2X case), but the small variation in this decrease fails to instill any order across the functionals. The spin-projected barriers still vary by 14.1 kcal mol⁻¹ when comparing the B3LYP and M06-2X numbers, implying that the issue with DFT representation of TS1 cannot be explained by the diradical character alone.

At this point we note an interesting trend visible in Tables 3, 4, and 7: the energy barrier of TS1 increases with the amount of exact (Hartree-Fock) exchange included in the hybrid functional. Taking Table 7 as an example, B3LYP contains 20% Hartree-Fock exchange and produces a barrier of 20.5 kcal mol⁻¹, while PBE0 contains 25% exact exchange and produces a barrier of 23.2 kcal mol⁻¹. On the opposite end of the spectrum, M06-2X contains 54% exact exchange and predicts a significantly higher barrier of 34.6 kcal mol⁻¹. This raises the question: can the percentage of exact exchange be

implicated in the wide variety of TS1 barriers predicted by the analyzed functionals?

Fig. 6 plots various quantities of TS1 as a function of the percentage of exact exchange, X, included in modified UB3LYP[X] functionals described in the Computational methods section and eqn (4). Each plot spans from 0% to 40% exact exchange (twice the amount included in the standard B3LYP functional). Fig. 6A shows a monotonic increase in the TS1 barrier as the percent exact exchange is increased, spanning from 9.6 to 29.3 kcal mol⁻¹. This plot alone implicates the percent of exact exchange in the variance observed across the reported functionals while the remaining three plots in Fig. 6 attempt to reconcile the additional effects the amount of exact exchange produces.

Fig. 6B shows a smooth increase in $\langle S^2 \rangle$ from 0 to 0.88 as the exact exchange increases. Interestingly, at 0% exact exchange there is no spin contamination in TS1, indicating all spin contamination arises due to the inclusion of Hartree-Fock exchange. The bond lengths of the forming bond, N-O2, and the breaking bond, O2-O3, both increase as a function of the Hartree-Fock exchange, though the breaking bond is relatively stagnant up to 20% exact exchange. The fact that both the forming and breaking bonds generally increase in length, shown in Fig. 6C, demonstrates some sort of repulsion between the far oxygen, O3, and the remaining heavy atoms. Fig. 6D reports the singlet-triplet gap which decreases monotonically and slowly flattens out at higher percentages of exact exchange, just as the TS1 barrier slows its increase.

As a final analysis of the effect of exact exchange, Fig. 7 presents the Mulliken spin densities as a function of the exact

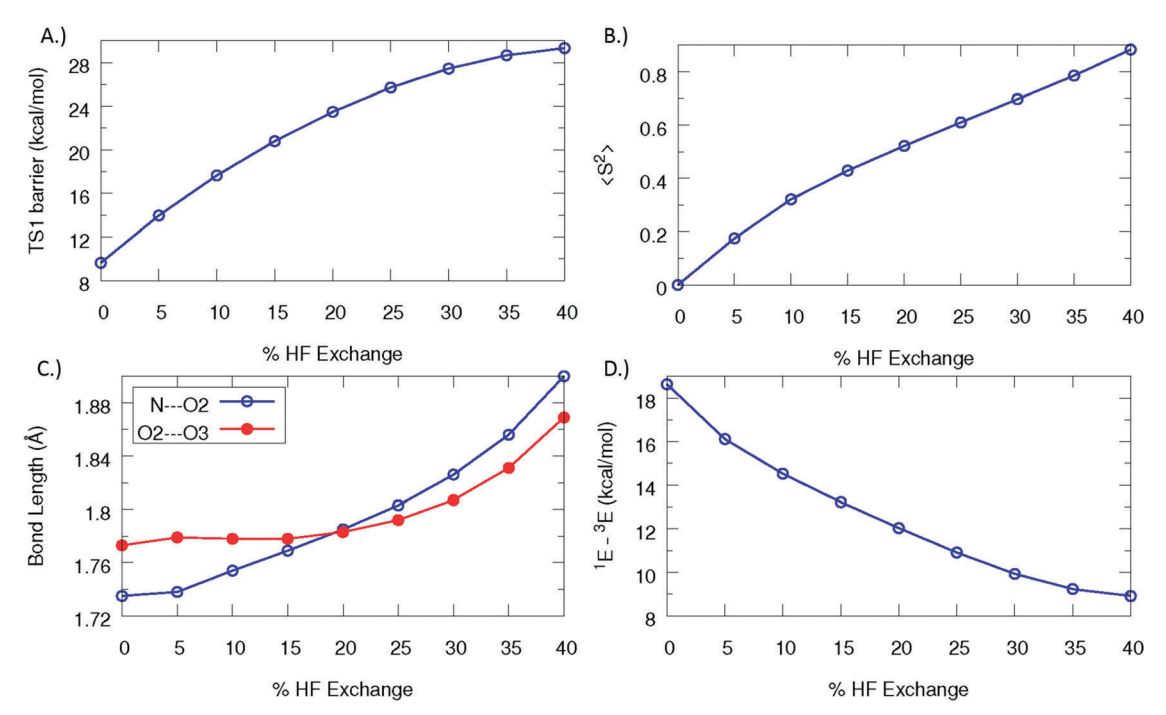


Fig. 6 Properties of TS1 with respect to percent exact Hartree-Fock exchange in UB3LYP[X] functionals. (A) TS1 barrier with respect to the reactant complex, (B) singlet $\langle S^2 \rangle$, (C) bond lengths of the forming and breaking bonds, (D) singlet-triplet gap.

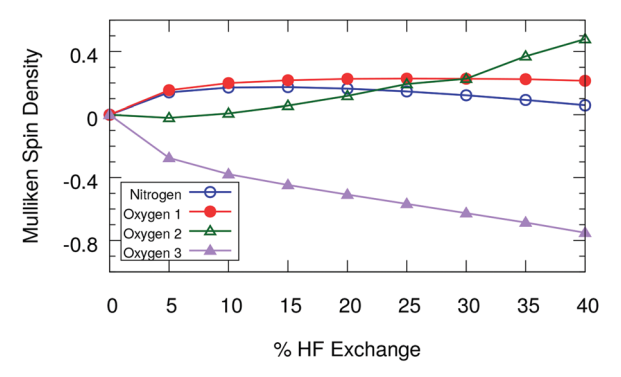


Fig. 7 Mulliken spin densities of TS1 with respect to exact Hartree–Fock exchange in UB3LYP[X] functionals. Oxygens labeled from left to right in Fig. 2. O1 corresponds to the nitroxyl oxygen, O2 the peroxide oxygen closest to the nitroxyl nitrogen, O3 the peroxide oxygen furthest from the nitrogen.

exchange in the UB3LYP[X] functionals. Here we see the far oxygen 3 spin density becomes more negative with exchange, hitting -0.75 at 40% exact exchange. The spin density on the bridging oxygen 2 increases with exact exchange, up to 0.48, and leads to a more direct interaction with oxygen 3. This increase in magnitude of the spin density coupled with the increase in spin contamination and decrease in singlet-triplet gap indicates an increase in diradical character as more exact exchange is added. The general increase in the TS1 barrier energy indicates the interaction between the two peroxide oxygens is unfavorable and the low B3LYP barriers are a result of suppressing this effect. The results seen in Fig. 6 and 7 imply that more accurate post-Hartree–Fock methods are likely to raise the TS1 barrier relative to the density functionals with a lower amount of exact exchange.

3.3. Post-Hartree-Fock methods

Table 8 reports the barriers of the transition state calculated using post-Hartree–Fock methods and B3LYP for comparison. All CCSD(T) and BD(T) calculations were performed as single points with the aug-cc-pVTZ basis set on the UB3LYP/aug-cc-pVQZ geometries. As expected, the CCSD(T) and BD(T) TS1

Table 8 Post-Hartree-Fock barriers^a

	B3LYP	UCCSD(T)	RCCSD(T)	UBD(T)	RBD(T)	CASSCF	NEVPT2
TS1	23.7	36.2	31.2	33.7	31.1	34.2	29.3
TS2-	23.2	23.8	23.8	23.7	23.7	27.0	23.3
grott							
TS2-	40.6	40.0	40.0	39.9	39.9	39.1	39.7
inter							
TS2-	56.9	55.6	55.6	55.6	55.6	59.1	54.6
intra							
TS3	12.8	11.8	11.9	11.9	11.9	12.4	10.7

^a Energies in kcal mol⁻¹ relative to associated complexes, as illustrated in Fig. 1. Geometries optimized at the UB3LYP/aug-cc-pVQZ level of theory, B3LYP energies at the aug-cc-pVQZ basis, both restricted and unrestricted CCSD(T) and BD(T) using aug-cc-pVTZ, CASSCF and NEVPT2 using (18,15) active space and extrapolated to aug-cc-pVTZ as described in the Methods section and eqn (1), uncorrected data available in the ESI.

barriers are significantly higher than the B3LYP result. Considering the instability in the restricted B3LYP wavefunction for TS1, one would expect an unrestricted Hartree-Fock reference wavefunction to be the appropriate choice for the correlated methods. However when using a UHF reference wavefunction, the coupled cluster TS1 barrier is 2.9 kcal mol⁻¹ higher than the BD(T) barrier, resulting from the effect of residual UHF spin contamination as seen in Table 5. Upon elimination of the first spin contaminant in the UHF treatment of TS1, the value of $\langle S^2 \rangle$ increases from 1.23 to 1.92 which implies contamination from a quintet state or higher. Spin contamination from spin states higher than a triplet is not expected to be accounted for by CCSD(T), however the orbital rotation step of the Brueckner method can better overcome such limitations.⁶⁰ This implies BD(T) is likely a better approximation of the TS1 barrier than the coupled cluster result when using a UHF reference.

Table 8 also reports the CCSD(T) and BD(T) barriers calculated with an RHF reference wavefunction, which significantly lowers the energy of TS1 in both cases. These results implicate high spin contamination in the UHF wavefunction as the culprit in the misbehavior of UCCSD(T), with the RCCSD(T) barrier only being 0.1 kcal mol⁻¹ higher than the RBD(T) barrier. The lowering of the BD(T) barrier is intriguing as we would expect the iterative process of removing the single excitations to settle on the RHF wavefunction, if it indeed provides a lower BD(T) energy. However, the converged reference with a UHF starting wavefunction still has a modest amount of spin contamination ($\langle S^2 \rangle = 0.489$). These results imply an RHF reference should be used in the case of high spin contamination when using CCSD(T), and BD(T) is still susceptible to error when such a high degree of spin contamination is present in the UHF reference. As expected, the BD(T) and CCSD(T) barriers are nearly identical across the other reactions, regardless of reference Hartree-Fock wavefunction. Additionally, the B3LYP barriers for the remaining transition states are hardly different from the BD(T) and CCSD(T) results, with the biggest difference being a 1.3 kcal mol⁻¹ decrease in the TS2-intra barrier.

Table 8 also reports the CASSCF(18,15) transition state barriers and the NEVPT2 values built off the CAS wavefunctions, both sets extrapolated to the aug-cc-pVTZ basis as described in the Methods section and eqn (1). The NEVPT2 treatment yields a barrier of 29.3 kcal mol⁻¹ for TS1, 5.6 kcal mol⁻¹ higher than the B3LYP value. Compared to UCCSD(T) and UBD(T), the UCCSD(T) TS1 barrier is 6.9 kcal mol⁻¹ higher than the NEVPT2 result while the UBD(T) barrier is 4.4 kcal mol⁻¹ higher than NEVPT2. This fits with our intuition of UBD(T) providing a more credible result than UCCSD(T). However, once a restricted wavefunction is used, the RCCSD(T) barrier for TS1 is only 1.9 kcal mol^{-1} higher than the NEVPT2 barrier. For the other transition states, we see the NEVPT2 values are in good agreement with the B3LYP values, the largest deviation being a decrease of 2.3 kcal mol⁻¹ in the case of TS2-intra. Given the NEVPT2 values, we see the first barrier as a slow formation of HNO2 and an endogenous water. The Grotthuss-like mechanism of TS2-grott is vastly favored over the other possibilities, with a barrier of 23.3 kcal mol⁻¹ to lead to

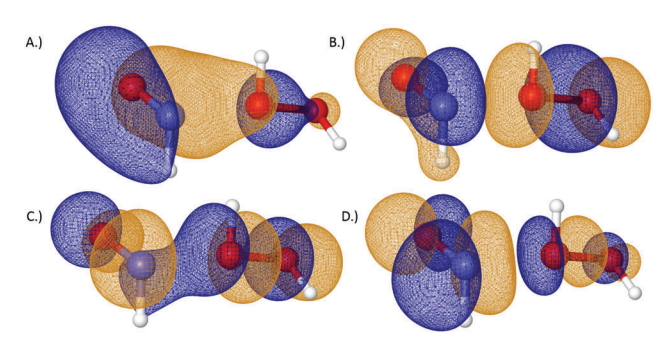


Fig. 8 CASSCF(18.15)/cc-pVDZ orbitals of TS1: (A) HOMO-1 with an occupation number of 1.92, (B) HOMO with an occupation number of 1.76, (C) LUMO with occupation number 0.26, and (D) LUMO+1 with occupation number 0.10.

trans-HONO, which can undergo a conformational change to cis-HONO with a barrier of 10.7 kcal mol⁻¹. Again, the conformational shift of HONO and the intramolecular HNO2 isomerization are in good agreement with the previous values in the literature as reported in Section 3.1.

As a final discussion of TS1, Fig. 8 reports the CASSCF(18,15)/ccpVDZ HOMO-1 to LUMO+1 molecular orbitals. What we refer to as the HOMO orbital (Fig. 8B) has an occupation of 1.76 and consists of a bonding combination along the breaking O-O bond and an antibonding combination along the forming N-O bond. The high occupation of a molecular orbital breaking the bond TS1 forms and forming the bond TS1 breaks leads to an overall increase in the barrier of TS1. The LUMO combination possesses the character one would expect for a favorable representation of this transition state: the nitrogen oxygen bond to be formed is covered by a bonding combination and the two peroxide oxygens are in an antibonding configuration. The LUMO orbital has an occupation number of 0.26 and the highest contributing configuration state function (CSF) beyond the ground state is a double excitation of the two electrons from the HOMO to the LUMO. This HOMO to LUMO CSF makes up 9% of the character of the overall wavefunction and prevents the progress of TS1 from being totally disfavored.

4. Conclusions

The goal of this work was to explore the potential reaction of hydrogen peroxide and nitroxyl. Both species have been implicated in reactions occurring in environmental processes, engineered systems, and in vivo. Through investigation using unrestricted B3LYP we found a reaction pathway linking the reactants hydrogen peroxide and nitroxyl to the formation of cis-HONO and water through three transition states. The first transition state, TS1, leads to HNO2 and an endogenous water through the splitting of the peroxide bond and a short proton transfer to the opposite peroxide oxygen. A high degree of spin contamination and significant diradical character on the open shell, singlet surface was found to cause wide variation in the TS1 barrier when calculated with a diverse set of hybrid density functionals. Through analysis using modified B3LYP[X] functionals, we identified the amount of exact exchange in the

individual functionals as an overwhelming factor in determining the barrier of, and degree of diradical character in, TS1. Further investigation with NEVPT2 on a CASSCF wavefunction produced a barrier of 29.3 kcal mol⁻¹ for TS1, significantly higher than the initial B3LYP result, but accessible under combustion conditions. BD(T) and CCSD(T) were also used in calculating the TS1 barrier and extrapolating the NEVPT2 results to a larger basis. Interestingly, an RHF wavefunction, while possessing an instability, needs to be used as the reference wavefunction in the correlation methods due to the high amount of spin contamination from spin states higher than a triplet in the TS1 UHF wavefunction. UCCSD(T) produces a TS1 barrier 6.9 kcal mol⁻¹ higher than the NEVPT2 value while the RCCSD(T) value is only 1.9 kcal mol⁻¹ higher.

The second step in the investigated reaction involves the isomerization of HNO2 to trans-HONO, which has been studied previously in the gas phase. 55-57 We found three mechanisms by which the HNO2 isomerization could proceed: the intramolecular gas phase mechanism, a proton shuttle mechanism utilizing the endogenous water, and a Grotthuss-like step donating and receiving a proton from the endogenous water. The NEVPT2 barrier for the intramolecular mechanism was found to be 54.6 kcal mol⁻¹, in good agreement with previous investigations. 55-58 The proton shuttle and Grotthuss mechanisms both improve over the previous results, with NEVPT2 barriers of 39.7 and 23.3 kcal mol^{-1} , respectively. The extremely low cost of the Grotthuss mechanism compared to the unimolecular rearrangement indicates the importance of including explicit water molecules when modeling the isomerization of HNO₂ to HONO, making it more accessible than previously thought. In fact, including a second water molecule in TS2-grott induces an extended Grotthuss mechanism for the isomerization with a B3LYP Gibbs free energy barrier of 15.5 kcal mol⁻¹, 6.1 kcal mol⁻¹ lower than TS2-grott at the same level of theory. Lastly, a previously-reported transition state linking trans-HONO to the slightly disfavored cis-HONO was explored with NEVPT2 and found to have a barrier of 10.7 kcal mol⁻¹, in good agreement with previous values. 61,62 Both the water-assisted HNO2 to cis-HONO and cis-to-trans isomerization of HONO are potentially accessible under physiological and environmental conditions.

Funding

K. Raghavachari is supported by the National Science Foundation [grant number CHE-1665427]. J. D. Raff is supported by the U.S. Department of Energy's Office of Science via their Biological and Environmental Research (BER) program (DE-SC0014443).

Conflicts of interest

There are no conflicts to declare.

Acknowledgements

The authors would like to thank the Big Red II supercomputing facility for computer time.

References

- 1 Ø. Skreiberg, P. Kilpinen and P. Glarborg, Ammonia chemistry below 1400 K under fuel-rich conditions in a flow reactor, *Combust. Flame*, 2004, **136**(4), 501–518.
- 2 W. C. Gardiner, *Gas Phase Combustion Chemistry*, Springer: New York, New York, 2nd edn, 2000, p. 543.
- 3 D. A. Dixon, J. S. Francisco and Y. Alexeev, Thermochemical Properties of HxNO Molecules and Ions from ab Initio Electronic Structure Theory, *J. Phys. Chem. A*, 2006, **110**(1), 185–191.
- 4 G. P. Robertson and P. M. Groffman, Nitrogen Transformation, in *Soil Microbiology, Biochemistry, and Ecology*, ed. E. A. Paul, Springer: New York, New York, 2007, pp. 341–364.
- 5 S. G. Cheskis, V. A. Nadtochenko and O. M. Sarkisov, Study of the HNO + HNO and HNO + NO reactions by intracavity laser spectroscopy, *Int. J. Chem. Kinet.*, 1981, 13(10), 1041–1050.
- 6 T. C. Brüggemann and F. J. Keil, Theoretical Investigation of the Mechanism of the Selective Catalytic Oxidation of Ammonia on H-Form Zeolites, *J. Phys. Chem. C*, 2009, **113**(31), 13860–13876.
- 7 W. Flores-Santana, D. J. Salmon, S. Donzelli, C. H. Switzer, D. Basudhar, L. Ridnour, R. Cheng, S. A. Glynn, N. Paolocci, J. M. Fukuto, K. M. Miranda and D. A. Wink, The Specificity of Nitroxyl Chemistry Is Unique Among Nitrogen Oxides in Biological Systems, *Antioxid. Redox Signaling*, 2011, 14(9), 1659–1674.
- 8 K. Pilegaard, Processes regulating nitric oxide emissions from soils, *Philos. Trans. R. Soc.*, *B*, 2013, **368**(1621), 20130126.
- 9 D. Fowler, M. Coyle, U. Skiba, M. A. Sutton, J. N. Cape, S. Reis, L. J. Sheppard, A. Jenkins, B. Grizzetti, J. N. Galloway, P. Vitousek, A. Leach, A. F. Bouwman, K. Butterbach-Bahl, F. Dentener, D. Stevenson, M. Amann and M. Voss, The global nitrogen cycle in the twenty-first century, *Philos. Trans. R.* Soc., B, 2013, 368(1621), 20130164.
- 10 S. Medinets, U. Skiba, H. Rennenberg and K. Butterbach-Bahl, A review of soil NO transformation: Associated processes and possible physiological significance on organisms, *Soil Biol. Biochem.*, 2015, 80, 92–117.
- 11 H. Su, Y. Cheng, R. Oswald, T. Behrendt, I. Trebs, F. X. Meixner, M. O. Andreae, P. Cheng, Y. Zhang and U. Pöschl, Soil Nitrite as a Source of Atmospheric HONO and OH Radicals, *Science*, 2011, 333(6049), 1616–1618.
- 12 R. Oswald, T. Behrendt, M. Ermel, D. Wu, H. Su, Y. Cheng, C. Breuninger, A. Moravek, E. Mougin, C. Delon, B. Loubet, A. Pommerening-Röser, M. Sörgel, U. Pöschl, T. Hoffmann, M. O. Andreae, F. X. Meixner and I. Trebs, HONO Emissions from Soil Bacteria as a Major Source of Atmospheric Reactive Nitrogen, *Science*, 2013, 341(6151), 1233.
- 13 N. K. Scharko, U. M. E. Schütte, A. E. Berke, L. Banina, H. R. Peel, M. A. Donaldson, C. Hemmerich, J. R. White and

- J. D. Raff, Combined Flux Chamber and Genomics Approach Links Nitrous Acid Emissions to Ammonia Oxidizing Bacteria and Archaea in Urban and Agricultural Soil, *Environ. Sci. Technol.*, 2015, **49**(23), 13825–13834.
- 14 R. C. Hudman, N. E. Moore, A. K. Mebust, R. V. Martin, A. R. Russell, L. C. Valin and R. C. Cohen, Steps towards a mechanistic model of global soil nitric oxide emissions: implementation and space based-constraints, *Atmos. Chem. Phys.*, 2012, 12(16), 7779–7795.
- 15 D. J. Arp, L. A. Sayavedra-Soto and N. G. Hommes, Molecular biology and biochemistry of ammonia oxidation by Nitrosomonas europaea, *Arch. Microbiol.*, 2002, 178(4), 250–255.
- 16 J. M. Poyatos, M. M. Muñio, M. C. Almecija, J. C. Torres, E. Hontoria and F. Osorio, Advanced Oxidation Processes for Wastewater Treatment: State of the Art, *Water, Air, Soil Pollut.*, 2009, 205(1), 187.
- 17 L. Chen, X. Li, J. Zhang, J. Fang, Y. Huang, P. Wang and J. Ma, Production of Hydroxyl Radical via the Activation of Hydrogen Peroxide by Hydroxylamine, *Environ. Sci. Technol.*, 2015, **49**(17), 10373–10379.
- 18 A. R. Ravishankara, J. S. Daniel and R. W. Portmann, Nitrous Oxide (N_2O): The Dominant Ozone-Depleting Substance Emitted in the 21st Century, *Science*, 2009, 326(5949), 123.
- 19 K. M. Miranda, The chemistry of nitroxyl (HNO) and implications in biology, *Coord. Chem. Rev.*, 2005, **249**(3), 433–455.
- 20 D. Basudhar, L. A. Ridnour, R. Cheng, A. H. Kesarwala, J. Heinecke and D. A. Wink, Biological signaling by small inorganic molecules, *Coord. Chem. Rev.*, 2016, 306(Part 2), 708–723.
- 21 J. M. Fukuto, A. S. Dutton and K. N. Houk, The Chemistry and Biology of Nitroxyl (HNO): A Chemically Unique Species with Novel and Important Biological Activity, *ChemBioChem*, 2005, **6**(4), 612–619.
- 22 C. H. Switzer, W. Flores-Santana, D. Mancardi, S. Donzelli, D. Basudhar, L. A. Ridnour, K. M. Miranda, J. M. Fukuto, N. Paolocci and D. A. Wink, The emergence of nitroxyl (HNO) as a pharmacological agent, *Biochim. Biophys. Acta, Bioenerg.*, 2009, 1787(7), 835–840.
- 23 P. Pagliaro, D. Mancardi, R. Rastaldo, C. Penna, D. Gattullo, K. M. Miranda, M. Feelisch, D. A. Wink, D. A. Kass and N. Paolocci, Nitroxyl affords thiol-sensitive myocardial protective effects akin to early preconditioning, *Free Radicals Biol. Med.*, 2003, 34(1), 33–43.
- 24 C.-u. Choe, J. Lewerenz, G. Fischer, T. F. Uliasz, M. G. Espey, F. C. Hummel, S. B. King, E. Schwedhelm, R. H. Böger, C. Gerloff, S. J. Hewett, T. Magnus and S. Donzelli, Nitroxyl exacerbates ischemic cerebral injury and oxidative neurotoxicity, *J. Neurochem.*, 2009, 110(6), 1766–1773.
- 25 X. L. Ma, F. Gao, G.-L. Liu, B. L. Lopez, T. A. Christopher, J. M. Fukuto, D. A. Wink and M. Feelisch, Opposite effects of nitric oxide and nitroxyl on postischemic myocardial injury, *Proc. Natl. Acad. Sci. U. S. A.*, 1999, 96(25), 14617–14622.
- 26 F. C. Kohout and F. W. Lampe, On the Role of the Nitroxyl Molecule in the Reaction of Hydrogen Atoms with Nitric Oxide, *J. Am. Chem. Soc.*, 1965, **87**(24), 5795–5796.

27 M. G. Bryukov, A. A. Kachanov, R. Timonnen, J. Seetula, J. Vandoren and O. M. Sarkisov, Kinetics of HNO reactions with O2 and HNO, Chem. Phys. Lett., 1993, 208(5), 392-398.

- 28 E. A. Veal, A. M. Day and B. A. Morgan, Hydrogen Peroxide Sensing and Signaling, Mol. Cell, 2007, 26(1), 1-14.
- 29 M. J. Frisch, G. W. Trucks, H. B. Schlegel, G. E. Scuseria, M. A. Robb, J. R. Cheeseman, G. Scalmani, V. Barone, G. A. Petersson, H. Nakatsuji, X. Li, M. Caricato, A. Marenich, J. Bloino, B. G. Janesko, R. Gomperts, B. Mennucci, H. P. Hratchian, A. F. Izmaylov, J. L. Sonnenberg, D. Williams-Young, F. Ding, F. Lipparini, F. Egidi, J. Goings, B. Peng, A. Petrone, J. V. Ortiz, V. G. Zakrzewski, J. Gao, N. Rega, G. Zheng, W. Liang, M. Hada, M. Ehara, K. Toyota, R. Fukuda, J. Hasegawa, M. Ishida, T. Nakajima, Y. Honda, O. Kitao, H. Nakai, T. Vreven, K. Throssell, J. A. Montgomery, Jr., J. E. Peralta, F. Ogliaro, M. Bearpark, J. J. Heyd, E. Brothers, K. N. Kudin, V. N. Staroverov, T. Keith, R. Kobayashi, J. Normand, K. Raghavachari, A. Rendell, J. C. Burant, S. S. Iyengar, J. Tomasi, M. Cossi, J. M. Millam, M. Klene, C. Adamo, R. Cammi, J. W. Ochterski, R. L. Martin, K. Morokuma, O. Farkas, J. B. Foresman and D. J. Fox, Gaussian 09 Revision E.01, Gaussian, Inc., Wallingford, CT, 2016.
- 30 F. Neese, The ORCA program system, Wiley Interdiscip. Rev.: Comput. Mol. Sci., 2012, 2(1), 73-78.
- 31 A. D. Becke, Density-functional thermochemistry. III. The role of exact exchange, J. Chem. Phys., 1993, 98(7), 5648-5652.
- 32 P. J. Stephens, F. J. Devlin, C. F. Chabalowski and M. J. Frisch, Ab Initio Calculation of Vibrational Absorption and Circular Dichroism Spectra Using Density Functional Force Fields, J. Phys. Chem., 1994, 98(45), 11623-11627.
- 33 C. Lee, W. Yang and R. G. Parr, Development of the Colle-Salvetti correlation-energy formula into a functional of the electron density, Phys. Rev. B: Condens. Matter Mater. Phys., 1988, 37(2), 785-789.
- 34 T. H. Dunning, Gaussian basis sets for use in correlated molecular calculations. I. The atoms boron through neon and hydrogen, J. Chem. Phys., 1989, 90(2), 1007-1023.
- 35 K. Fukui, The path of chemical reactions the IRC approach, Acc. Chem. Res., 1981, 14(12), 363-368.
- 36 H. P. Hratchian and H. B. Schlegel, Accurate reaction paths using a Hessian based predictor-corrector integrator, J. Chem. Phys., 2004, 120(21), 9918-9924.
- 37 H. P. Hratchian and H. B. Schlegel, Using Hessian Updating To Increase the Efficiency of a Hessian Based Predictor-Corrector Reaction Path Following Method, J. Chem. Theory Comput., 2005, 1(1), 61-69.
- 38 V. Barone and M. Cossi, Quantum Calculation of Molecular Energies and Energy Gradients in Solution by a Conductor Solvent Model, J. Phys. Chem. A, 1998, 102(11), 1995-2001.
- 39 M. Cossi, N. Rega, G. Scalmani and V. Barone, Energies, structures, and electronic properties of molecules in solution with the C-PCM solvation model, J. Comput. Chem., 2003, 24(6), 669-681.
- 40 Y. Zhao and D. G. Truhlar, The M06 suite of density functionals for main group thermochemistry, thermochemical

- kinetics, noncovalent interactions, excited states, and transition elements: two new functionals and systematic testing of four M06-class functionals and 12 other functionals, Theor. Chem. Acc., 2008, 120(1), 215-241.
- 41 C. Adamo and V. Barone, Toward reliable density functional methods without adjustable parameters: The PBE0 model, J. Chem. Phys., 1999, 110(13), 6158-6170.
- 42 S. Grimme, J. Antony, S. Ehrlich and H. Krieg, A consistent and accurate ab initio parametrization of density functional dispersion correction (DFT-D) for the 94 elements H-Pu, J. Chem. Phys., 2010, 132(15), 154104.
- 43 S. Grimme, S. Ehrlich and L. Goerigk, Effect of the damping function in dispersion corrected density functional theory, J. Comput. Chem., 2011, 32(7), 1456-1465.
- 44 T. Yanai, D. P. Tew and N. C. Handy, A new hybrid exchange-correlation functional using the Coulombattenuating method (CAM-B3LYP), Chem. Phys. Lett., 2004, 393(1), 51-57.
- 45 J.-D. Chai and M. Head-Gordon, Long-range corrected hybrid density functionals with damped atom-atom dispersion corrections, Phys. Chem. Chem. Phys., 2008, 10(44), 6615-6620
- 46 K. Raghavachari, G. W. Trucks, J. A. Pople and M. Head-Gordon, A fifth-order perturbation comparison of electron correlation theories, Chem. Phys. Lett., 1989, 157(6), 479-483.
- 47 J. F. Stanton, Why CCSD(T) works: a different perspective, Chem. Phys. Lett., 1997, 281(1), 130-134.
- 48 N. C. Handy, J. A. Pople, M. Head-Gordon, K. Raghavachari and G. W. Trucks, Size-consistent Brueckner theory limited to double substitutions, Chem. Phys. Lett., 1989, 164(2), 185-192.
- 49 C. Angeli, R. Cimiraglia, S. Evangelisti, T. Leininger and J. P. Malrieu, Introduction of *n*-electron valence states for multireference perturbation theory, J. Chem. Phys., 2001, 114(23), 10252-10264.
- 50 C. Angeli, R. Cimiraglia and J.-P. Malrieu, *n*-electron valence state perturbation theory: A spinless formulation and an efficient implementation of the strongly contracted and of the partially contracted variants, J. Chem. Phys., 2002, **117**(20), 9138–9153.
- 51 V. Veryazov, P. Å. Malmqvist and B. O. Roos, How to select active space for multiconfigurational quantum chemistry?, Int. J. Quantum Chem., 2011, 111(13), 3329-3338.
- 52 K. Yamaguchi, F. Jensen, A. Dorigo and K. N. Houk, A spin correction procedure for unrestricted Hartree-Fock and Møller-Plesset wavefunctions for singlet diradicals and polyradicals, Chem. Phys. Lett., 1988, 149(5), 537-542.
- 53 E. Goldstein, B. Beno and K. N. Houk, Density Functional Theory Prediction of the Relative Energies and Isotope Effects for the Concerted and Stepwise Mechanisms of the Diels-Alder Reaction of Butadiene and Ethylene, J. Am. Chem. Soc., 1996, 118(25), 6036-6043.
- 54 D. C. Ashley and M.-H. Baik, The Electronic Structure of [Mn(V)=O]: What is the Connection between Oxyl Radical Character, Physical Oxidation State, and Reactivity?, ACS Catal., 2016, 6(10), 7202-7216.

55 S.-y. Takane and T. Fueno, Electronic structure and the hydrogen-shift isomerization of hydrogen nitryl HNO2, Theor. Chim. Acta, 1994, 87(6), 431-439.

- 56 S. Berski, Z. Latajka and A. J. Gordon, Ab Initio and Quantum Chemical Topology studies on the isomerization of HONO to HNO2. Effect of the basis set in QCT, I. Comput. Chem., 2010, 31(14), 2555-2567.
- 57 M. T. Nguyen, R. Sumathi, D. Sengupta and J. Peeters, Theoretical analysis of reactions related to the HNO2 energy surface: OH + NO and H + NO2, Chem. Phys., 1998, 230(1), 1-11.
- 58 S. H. Mousavipour and S. S. Asemani, Theoretical Study on the Dynamics of the Reaction of HNO(1A') with HO2(2A"), J. Phys. Chem. A, 2015, 119(22), 5553-5565.

- 59 R. Asatryan, J. W. Bozzelli and J. M. Simmie, Thermochemistry for enthalpies and reaction paths of nitrous acid isomers, Int. J. Chem. Kinet., 2007, 39(7), 378-398.
- 60 W. Chen and H. B. Schlegel, Evaluation of S2 for correlated wave functions and spin projection of unrestricted Møller-Plesset perturbation theory, J. Chem. Phys., 1994, 101(7), 5957-5968.
- 61 L. H. Jones, R. M. Badger and G. E. Moore, The Infrared Spectrum and the Structure of Gaseous Nitrous Acid, J. Chem. Phys., 1951, 19(12), 1599-1604.
- 62 R. T. Hall and G. C. Pimentel, Isomerization of Nitrous Acid: An Infrared Photochemical Reaction, J. Chem. Phys., 1963, 38(8), 1889-1897.